

Addressing electron spins embedded in metallic graphene nanoribbons

Niklas Friedrich,¹ Rodrigo E. Menchón,² Iago Pozo,³ Jeremy Hieulle,¹ Alessio Vegliante,¹ Jingcheng Li,¹ Daniel Sánchez-Portal,^{2,4} Diego Peña,^{3,*} Aran Garcia-Lekue,^{2,5,†} and José Ignacio Pascual^{1,5,‡}

¹*CIC nanoGUNE-BRTA, 20018 Donostia-San Sebastián, Spain*

²*Donostia International Physics Center (DIPC), 20018 Donostia-San Sebastián, Spain*

³*CiQUS, Centro Singular de Investigación en Química Biolóxica e Materiais Moleculares, 15705 Santiago de Compostela, Spain*

⁴*Centro de Física de Materiales CSIC-UPV/EHU, 20018 Donostia-San Sebastián, Spain*

⁵*Ikerbasque, Basque Foundation for Science, 48013 Bilbao, Spain*

(Dated: June 16, 2022)

Spin-hosting graphene nanostructures are promising metal-free systems for elementary quantum spintronic devices. Conventionally, spins are protected from quenching by electronic bandgaps, which also hinder electronic access to their quantum state. Here, we present a narrow graphene nanoribbon substitutionally doped with boron heteroatoms that combines a metallic character with the presence of localized spin 1/2 states in its interior. The ribbon was fabricated by on-surface synthesis on a Au(111) substrate. Transport measurements through ribbons suspended between the tip and the sample of a scanning tunnelling microscope revealed their ballistic behavior, characteristic of metallic nanowires. Conductance spectra show fingerprints of localized spin states in form of Kondo resonances and inelastic tunnelling excitations. Density functional theory rationalizes the metallic character of the graphene nanoribbon due to the partial depopulation of the valence band induced by the boron atoms. The transferred charge builds localized magnetic moments around the boron atoms. The orthogonal symmetry of the spin-hosting state's and the valence band's wavefunctions protects them from mixing, maintaining the spin states localized. The combination of ballistic transport and spin localization into a single graphene nanoribbon offers the perspective of electronically addressing and controlling carbon spins in real device architectures.

Graphene nanoribbons (GNRs) are narrow stripes of graphene a few nanometer wide. In spite of graphene being inherently a semimetallic material, electronic correlations and confinement of their electrons into one dimension generally result in gapped band structures [1, 2]. Since the bandgap depends on the GNR's orientation, edge and width [2–6], precise control of their semiconducting character can be achieved by on-surface synthesis methods [6–10].

In the last years it has been proposed that GNRs can also host localized spin states at specific positions of their carbon lattice, turning them into potential candidates for metal-free spintronic devices [11–14]. Spin states have been found in GNRs and in graphene nanoflakes, mostly localized around zig-zag edges and various types of defects [15–34]. Two-terminal electronic transport measurements using a scanning tunnelling microscope (STM) have demonstrated that spins can be addressed by electrons tunnelling through the GNR's bandgap [23, 35]. Although a bandgap favors spin localization, it restricts low-energy electron movement to distances of a few angstroms. This limits the integration of spin-hosting GNRs into spintronic devices. Ballistic transport through metallic GNRs [36–38] would ease the implementation by facilitating the read out of the embedded spins.

Here, we report on the detection of localized spins in metallic GNRs realized by substitutionally doping a narrow-bandgap GNR with boron atoms in its interior. The boron heteroatoms turn the ribbon metallic and, at

the same time, acquire a net magnetic moment. Density functional theory (DFT) calculations reveal that the spin is protected from the partially filled valence band (VB) by the different symmetry of the VB and the boron bands. Pentagonal defects, as those observed in the experiment, break the structural symmetry and open small hybridization gaps in the VB close to the Fermi level. We combined two-terminal transport experiments with differential conductance (dI/dV) spectroscopy to probe the electronic and magnetic properties of individual GNRs. Ballistic transport was stable over distances of several nanometers. The presence of a Kondo resonance proves access to the spin at a transport length of more than 3 nm.

RESULTS AND DISCUSSION

Simulations of the electronic structure of a metallic graphene nanoribbon. The atomic structure of the investigated ribbon is derived from that of a 7-atom wide armchair GNR (7aGNR) with substitutional boron doping at periodic intervals [39–45]. Here, we modified the edge structure and width of the undoped 7aGNR by periodically alternating five and seven carbon atom wide segments (575-aGNR, Figure 1a). DFT calculations of the electronic band structure, shown in Figure 1b, predict that the undoped GNR has a small bandgap, with no spin polarization. Interestingly, the wavefunction of both valence and conduction bands are antisymmetric with respect to the central axis of the ribbon (Figure

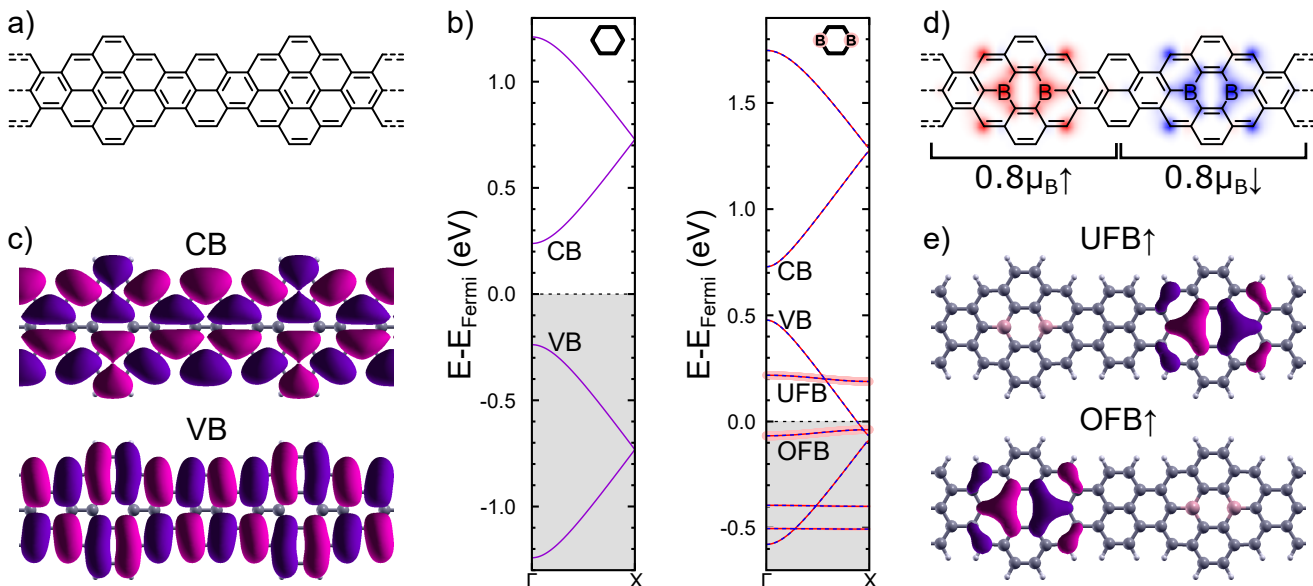


FIG. 1. (a) Lewis structure of the proposed 575-aGNR without boron doping. (b) Spin-polarized DFT calculated band structure of the 575-aGNR and the 2B-575-aGNR using a doubled supercell like shown in panel (a). Boron character of the bands is indicated by a pink shadow. (c) DFT calculated wavefunctions at Γ of the CB and VB of the 575-aGNR. (d) Lewis structure of the 2B-575-aGNR shown on top of a color map representing the calculated spin-polarization density. (e) DFT calculated wavefunctions at Γ of the spin-up unoccupied (UFB) and occupied (OFB) boron flat band of the 2B-575-aGNR.

1c), in contrast with the symmetric character of frontier bands in the related 7aGNR [43]. This change in the bands' symmetry turns out to be crucial to understand the effect of boron substitution inside the GNR.

Substituting the two central carbon atoms in the wider segments with boron atoms (as shown in Figure 1d) creates two boron-rich flat bands. These bands originate from pure boron orbitals and have no topological character, unlike the flat bands of 2B-7aGNRs [23, 43]. The band structure of the 2B-575-aGNR, also shown in Figure 1b, reveals a significant charge transfer from its VB to the boron bands, resulting in an occupied flat band (OFB), hosting approximately 2 electrons, and an unoccupied flat band (UFB). The VB is partially depopulated and becomes metallic.

The boron flat bands and VB cross without opening a gap, as shown in Figure 1b, revealing a negligible mixing. This is a consequence of the different symmetries of their wavefunctions (Figure 1c, e). The boron flat bands, localized around the boron atoms, are symmetric with respect to the central ribbon axis, while the VB is anti-symmetric. The orthogonality between VB and boron flat bands allows electrons in the VB to propagate unperturbed along the ribbon [41], resulting in a metallic band and maintaining the boron states localized around the diboron impurities. DFT finds a magnetic moment of $0.8\mu_B$, close to spin $S = 1/2$, associated with the OFB that is localized around each 2B-unit. Spin moments in adjacent 2B-units tend to anti-align, as shown in Figure 1d, so the periodic system shows no net spin-

polarization.

On-surface synthesis of 2B-575-aGNRs. Based on the intriguing properties predicted by DFT calculations, we decided to explore the on-surface synthesis and characterization of this boron-doped GNR. A retrosynthetic analysis identified the compound shown in Figure 2a as the ideal molecular precursor, which might lead to the formation of 2B-575-aGNRs by sequential Ullmann coupling and cyclodehydrogenation reactions on a Au(111) substrate. The molecular precursor was obtained by solution chemistry in one step from easily available starting materials (see Supporting Information (SI) for details) and sublimated *in situ* on Au(111). Polymerization occurs at 250 °C, a higher temperature than for other systems [7, 40], and close to the onset of cyclodehydrogenation of the polymer. The presence of the precursor's bulky methyl groups increases the energy barrier for the formation of metal organic complexes [46], which have been shown to facilitate the on-surface Ullmann coupling [47]. As a consequence, the Ullmann coupling requires a higher temperature for activation. We annealed the sample to 300 °C to achieve a high amount of planar ribbons. The resulting structures were mostly curved and interlinked ribbons, as seen in Figure 2b, with a few short and straight segments (red arrows). Figure 2c shows an STM image of a single straight 2B-575-aGNR segment, where four boron doping sites can be identified as wider and darker segments of the ribbon.

Two-terminal electronic transport measurements. We studied the electronic transport through a

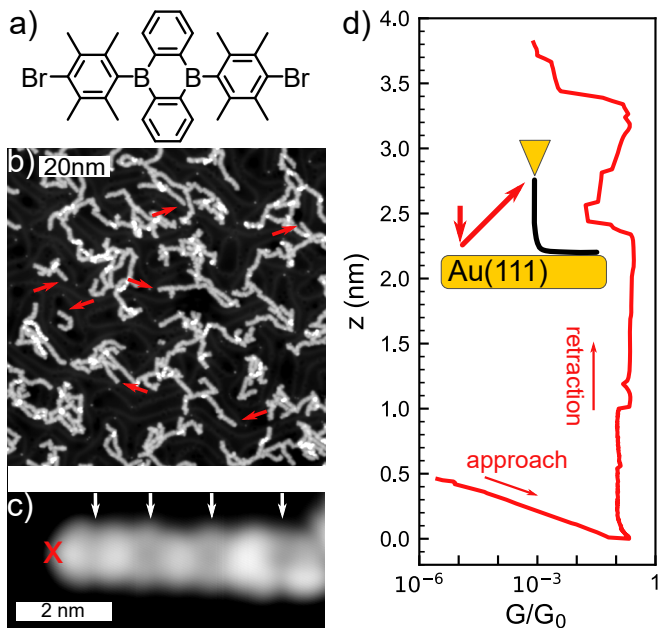


FIG. 2. (a) Molecular precursor used for synthesizing the 2B-575-aGNRs. (b) STM topography image ($V = 1\text{ V}$, $I = 30\text{ pA}$). Straight 2B-575-aGNRs are indicated by red arrows. (c) STM topography image ($V = -300\text{ mV}$, $I = 30\text{ pA}$) of a four precursor unit long 2B-575-aGNR. The positions of boron doping are indicated by white arrows. The red cross indicates the position from where the GNR is lifted for the transport experiment. (d) $G(z, V = 10\text{ mV})$ for the GNR presented in (c). The conductance is independent of z up to $z \approx 2.2\text{ nm}$. The inset is a schematic drawing of the experimental setup.

GNR suspended between the tip and sample of an STM [18, 23, 35, 48–50]. To reach this two-terminal configuration, we positioned the tip above the apex of the 2B-575-aGNR (red cross in Figure 2c) and approached the tip towards the substrate until a sudden increase in the current indicated the formation of a bond between tip and ribbon. Then, we retracted the tip following a leaned trajectory along the backbone of the ribbon. This procedure lifts the 2B-575-aGNR partially from the Au(111) and electronically decouples the free-standing segment from the metal.

Electronic transport measurements through the lifted ribbons confirm that they behave as ballistic conductors. As shown in Figure 2d, the linear conductance $G(z)$ of the ribbon remains constant for several nanometers while the tip is retracted. The constant conductance contrasts with the exponentially decaying conductance found for semiconducting ribbons [23, 35, 48, 51]. In a ballistic conductor, the electron transmission \mathcal{T} remains constant as a function of its length, and the conductance per channel amounts to $\mathcal{T}G_0$, where $G_0 = e^2/\pi\hbar = 77.5\text{ }\mu\text{S}$ is the conductance quantum. In the results shown in Figure 2, we observe high conductance values around $\sim 0.2G_0$ remaining constant for more than 2 nm of GNR elevation. The electron transmission smaller than G_0 is probably

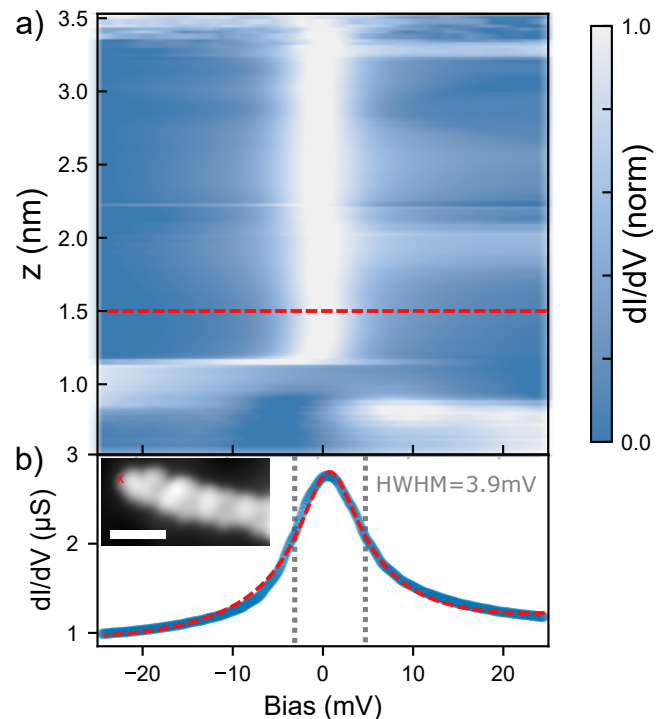


FIG. 3. (a) Normalized $dI/dV(V, z)$ -map (see methods for details on normalization procedure). A zero-bias resonance appears in the spectra for $z > 1.2\text{ nm}$. (b) One example dI/dV -spectrum (blue) fitted with a Frotta function [55] (red dashed line). The spectrum was taken at $z = 1.5\text{ nm}$. Inset: STM topography image ($V = -300\text{ mV}$, $I = 30\text{ pA}$, scale bar is 2 nm). The red cross indicates the position from where the GNR is lifted.

caused by the finite contact resistance between tip and GNR [52, 53]. At some points we find small variations of the conductance around $0.1G_0$, which are consistent with atomic-scale rearrangements of the GNR-electrode contacts when additional borylated units detach from the surface [48, 54]. The ballistic electron transport found here reflects the existence of scattering free transmission channels in free-standing 2B-575-aGNRs, in agreement with the boron induced metallic character revealed by our DFT calculations in Figure 1.

Observation of the Kondo effect in ballistic ribbons. Figure 3a shows a $dI/dV(V, z)$ spectral map obtained by measuring dI/dV spectra during the lift of a 2B-575-aGNR (inset Figure 3b). A narrow zero-bias resonance (HWHM = 3.2 mV) appears suddenly at $z = 1.2\text{ nm}$ and prevails up to $\Delta z \geq 3.5\text{ nm}$ during the lifting procedure. We interpret this resonance as a manifestation of the Kondo effect in the electronic transport through the ribbon [56]. The Kondo resonance is the fingerprint of a spin state weakly coupled to an electron bath [15, 18, 21, 23, 57–59]. Here, it is observed for more than 2 nm during the GNR elevation, hinting that the Kondo screening is not simply mediated by electrons at the surface [23]. We suggest that the metallic band of

the ribbon is responsible for the screening of the localized magnetic moments.

In the transport experiments presented in Figure 2 and 3 we found electronic and magnetic fingerprints that are consistent with our DFT calculations of the 2B-575-aGNR. All the 19 ribbons explored in this manner show similar results, in every case reproducing segments of constant conductance associated to ballistic transport, and Kondo resonances. However, many ribbons also showed a step-wise decrease in their conductance plots at some elongations, which we attribute to the presence of defects in their structure.

Role of atomic defects on the nanoribbons. To detect the presence of atomic-scale defects in 2B-575-aGNRs, we measured constant height current images using a CO-functionalized tip [60, 61]. The image of a nanoribbon composed of 4 molecular units (*i.e.* 4 boron dimers) is shown in Figure 4a. It is consistent with a ribbon containing a sequence of pentagonal rings in its carbon backbone at the position of Ullmann coupling (white arrows in Figure 4a). The extracted Lewis structure of the ribbon (referred to as 2B-575*-aGNR) is shown in Figure 4b. Pentagonal rings are known to appear when methyl groups of the precursor detach during the polymerization reaction [17, 24, 62]. This type of defect at the linking position is the most common structure we find in an analysis of 16 ribbons.

To unravel the effect of the atomic defects on the electronic transport of 2B-575-aGNRs, we performed two-terminal transport measurements on the ribbon shown in Figure 4 in a suspended geometry. As depicted in Figure 4c, the conductance $G(z)$ decreases step-wise with increasing z . The conductance steps are spaced by $\Delta z \sim 1.4$ nm, matching with the distance between two diboron sites. This suggests that they appear when a new precursor unit is inserted in the free-standing part of the ribbon [54].

Between conductance steps, constant conductance plateaus unveil that some ballistic behavior is retained. However, now, we found three qualitatively different regimes, depicted in Figure 4d. First, we observed a metallic like behavior, with flat $dI/dV \sim 0.3G_0$ signal persisting until $z = 0.6$ nm, where the first conductance steps appears. Upon further tip retraction, a zero-bias resonance similar to the one shown in Figure 3 appears in the spectra. Again, this indicates that a localized spin appears in the free-standing segment of the ribbon. This Kondo feature disappears at $z = 1.75$ nm, coinciding with a second step in the linear conductance plot of Figure 4c. Above this z value, spectra exhibit two bias-symmetric dI/dV steps, characteristic of inelastic electron tunnelling (IET) excitations.

To follow the IET spectral evolution during the retraction, we show in Figure 4e a normalized $d^2I/dV^2(V, z)$ -map. We observe that at $z = 1.75$ nm the Kondo resonance splits gradually in ≤ 1 Å and converts into IET

steps (see SI Figure 4). Above this value, the steps are observed for more than 3 nm retraction with small variations of their excitation energy. A fainter dI/dV -step, at approximately 45 mV larger bias voltage, can also be observed in the spectra above 3 nm. The continuous evolution from Kondo to IET excitations suggests that a complex spin texture exists in the 2B-575*-aGNR.

DFT calculations for periodic 2B-575*-aGNRs revealed that the presence of the pentagonal rings in the ribbon has two important implications. First, they break the structural symmetry of the GNR, mixing the wavefunctions of boron flat bands and VB. Now, the band structure in Figure 4f shows avoided crossings of both UFB and OFB with the VB, characteristic of a small hybridization. Second, the removal of a carbon atom from the ribbon effectively injects another hole and lowers the occupation of both the VB and the OFB. Since the VB still crosses the Fermi level, the ribbon preserves its metallic character. DFT pictures the depopulation of the OFB as a mean delocalization of an electron over several 2B-units and a smaller net magnetic moment associated with each diboron unit ($\sim 0.5\mu_B/2B$).

To interpret the experimental IET signal, we explored different magnetic states obtained by DFT simulations of finite ribbons, like the one presented in Figure 4g (see SI Figure 7). DFT results indicate that the system cannot be simply treated as Heisenberg-like Hamiltonian due to the electron delocalization. In fact, DFT significantly underestimates the excitation energies as compared to the measured IET spectra and did not fully capture the relevant physical mechanisms behind the inelastic steps.

Given that the hybridization between the VB and the boron flat bands is small (notice in Figure 4f the 1 to 10 ratio between the size of the hybridization gaps and the VB band width), a valid approximation is treating VB and OFB as two different subsystems, disregarding excitations that imply charge-transfer between them. The observed spectral steps can then be attributed to inelastic excitations in the OFB/UFB subsystem induced by conduction electrons propagating through the VB. To describe the excitation spectrum of the boron flat bands, we use a Hubbard model with parameters t and U obtained from the DFT band structure in Figure 4f. This simple model can be exactly solved and approximately accounts for electron correlations in the excitation spectrum. Based on the OFB's occupation observed in DFT calculations (see Figure 4f), we consider the probable case of two electrons distributed over four electron sites.

Exact diagonalization of the Hubbard Hamiltonian leads to the energy spectrum presented in Figure 4g. The ground state is a singlet combination of the two spins. The first excited state is a triplet state located at $E_1 = 94$ meV, which matches reasonably well with the energy of the first excitation step in our experiments. Furthermore, the model also finds an excited singlet state at $E_2 = 145$ meV, in strong coincidence with the second

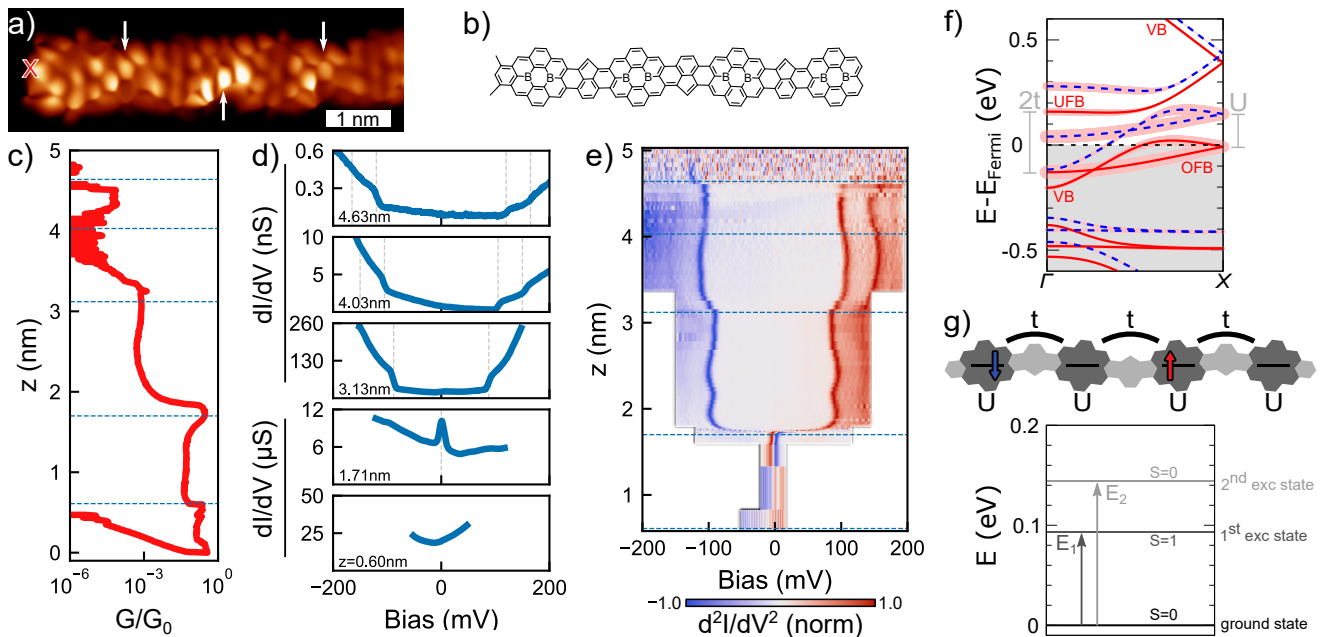


FIG. 4. (a) Bond-resolved constant height current image ($V = 5$ mV). The 2B-units alter the contrast due to buckling of the ribbon. Pentagons are indicated by white arrows. The red cross indicates the position from where the ribbon is lifted. (b) Lewis structure of the 2B-575*-aGNR in (a). (c) Linear conductance $G(z, V = 10$ mV) obtained while lifting the ribbon presented in (a). Some ballistic behavior is retained. (d) dI/dV -spectra at selected z . The values are indicated and correspond to the blue, dotted lines in (c) and (e). A single Kondo-resonance at $z = 1.71$ nm indicates the presence of a spin $S = 1/2$. For larger z inelastic excitations dominates the spectra. (e) Normalized $d^2I/dV^2(V, z)$ -map obtained by numerical differentiation (see methods for details on normalization procedure). (f) DFT calculated band structure of periodic 2B-575*-aGNR. Notice that in this case the unit cell necessarily contains two 2B-units. Red and blue bands correspond to spin up and down. Boron character of the bands is indicated by a pink shadow. The corresponding band from the 2B-575-aGNR is indicated for the spin up band. (g) Hubbard-model used to calculate spin-excitations of the finite sized system and its energy spectrum for two electrons that are delocalized across four hopping sites. $U = 155.9$ meV, $t = 133.9$ meV, obtained from (f).

spectral IET step. The observed agreement between the calculated and experimentally observed excitation energies indicates the IET signals can be due to electron-hole pair excitations of a partially populated flat band, a similar excitation process to the one recently observed on small molecules on insulating layers [63]. This interpretation is supported by the fact that the excitation energies in the model are dominated by the hopping parameter between two 2B-sites t and are stable against changes of U (SI Figure 5) or electron occupation (SI Figure 6). This explains why the step values are relatively independent from the length of the free-standing segment. The model unveils a probable source of scattering phenomena in the electronic transport, which, also, can be responsible for the step-wise decrease of the linear conductance found when a new diboron unit is lifted from the surface (Figure 4c).

CONCLUSIONS

We have presented a graphene nanoribbon that combines a metallic transport band with localized spins inside, and described experimental fingerprints of both the

metallic character and the spin-polarized states. The ribbon is fabricated by substitutionally doping the narrow-bandgap 575-aGNR with diboron units. DFT simulations unveiled that the dispersive VB becomes partially depopulated by donating electrons to flat bands formed by the diboron units. As a result, single spins emerge localized at every diboron unit, protected from the VB by their different wavefunction symmetry. Two-terminal transport experiments through free-standing GNRs placed between tip and sample of an STM demonstrated ballistic electron transport, transmitting electrons with a constant value of $0.2G_0$ for a free-standing segment length of a few nanometers. Simultaneously, the differential conductance spectroscopy in the transport configuration unraveled the spin localization by revealing a Kondo resonance that was stable during the elevation of the GNR from the surface.

In addition to the ideal case, we found that atomic defects such as pentagonal rings in the structure, frequently found in our experiments, enable a small wavefunction mixing between VB and the boron flat bands and partially depopulate both bands. The effect of these pentagonal defects in the transport is drastic, because it enables

a finite interaction between adjacent diboron units and delocalizes the electrons along the partially occupied flat band. We found that the ballistic character of the ribbon partly survives in the presence of pentagonal defects, but a new inelastic excitations appears in the spectra, accompanying a step-wise decrease of the linear conductance with ribbon elevation. Through a simple Hubbard model, parameterized with results from the DFT simulations, we found that the inelastic spectral features can be attributed to excitation of the many-body states of the partially depopulated flat band. These results thus demonstrate that the 2B-575-aGNR represent a unique molecular system to import flat band phenomena into one-dimensional graphene nanoribbons, envisioning the study of the underlying electron transport phenomena present in these correlated systems.

EXPERIMENTAL AND METHODS

Sample preparation. A Au(111) single crystal was prepared by Ne⁺ sputtering and successive annealing at $T = 450^\circ\text{C}$ under ultra-high vacuum conditions. The precursor molecules were sublimated *in situ* from a Knudsen cell at a temperature of 220°C . Afterwards the gold was annealed to $T = 180^\circ\text{C}$ for 10 minutes and flashed to $T = 300^\circ\text{C}$ for one minute. The samples were analyzed in a custom-made low-temperature STM at 5 K. The Figures presenting experimental data were prepared using WSxM [64] and the python matplotlib library [65] using perceptual continuous color scales [66].

Differential conductance measurements. Spectroscopic dI/dV -measurements were performed using an external lock-in amplifier with frequency $f = 867.6\text{ Hz}$, time constant $\tau = 30\text{ ms}$ and modulation $V_{\text{mod}} = 2\text{ mV}$. The $G(V, z)$ -map in Figure 3a is normalized for each $z = z_0$ separately, using the formula $G_{\text{norm}}(V, z_0) = (G(V, z_0) - G_{\text{min}})/(G_{\text{max}} - G_{\text{min}})$, where $G(V, z_0)$ is the differential conductance and $G_{\text{max}(\text{min})}$ the maximum (minimum) value of $G(V, z_0)$. The d^2I/dV^2 -map in Figure 4e is normalized equivalently using $G'_{\text{norm}}(V, z_0) = G'(V, z_0)/|G'_{\text{min}(\text{max})}|$, where G' is the derivative of the conductance and $G'_{\text{min}(\text{max})}$ is the minimum (maximum) of G' . $G'_{\text{min}(\text{max})}$ was used for negative (positive) values of $G'(V)$.

Density functional theory calculations. First-principles electronic structure calculations were performed using DFT as implemented in the SIESTA software package[67, 68]. The van der Waals density functional by Dion *et al.* [69] with the modified exchange correlation by Klimeš, Bowler and Michaelides[70] was used. The valence electrons were described by a double- ζ plus polarization (DZP) basis set with the orbital radii defined using a 54 meV energy shift [68], while the core electrons were described using norm-conserving Trouillers-Martins

pseudopotentials [71]. For integrations in real space[68] an energy cutoff of 300 Ry was used. The smearing of the electronic occupations was defined by an electronic temperature of 300 K with a Fermi-Dirac distribution. The self-consistency cycles were stopped when variations on the elements of both the density matrix and the Hamiltonian matrix were smaller than 10^{-4} eV . In order to avoid interactions with periodic images from neighboring cells, systems were calculated within a simulation cell where at least 50 Å of vacuum space was considered. Variable cell relaxations and geometry optimizations were performed using the conjugate gradient method using a force tolerance equal to $10\text{ meV}/\text{Å}$ and 0.2 GPa as a stress tolerance. For periodic ribbons, a 40 k-point mesh along the GNRs' periodic direction was used.

ACKNOWLEDGMENTS

We gratefully acknowledge financial support from Spanish AEI and the European Regional Development Fund (ERDF) and the Maria de Maeztu Units of Excellence Program and from the European Union (EU) through Horizon 2020 (FET-Open project SPRING Grant. no. 863098). We thank the Spanish Agencia Estatal de Investigación (PID2019-107338RB-C62, PID2019-110037GB-I00 and PCI2019-111933-2 and Xunta de Galicia (Centro de Investigación de Galicia accreditation 2019–2022, ED431G 2019/03) and Dpto. Educación Gobierno Vasco (Grant No. PIBA-2020-1-0014) and Programa Red Guipuzcoana de Ciencia, Tecnología e Innovación 2021 (Grant Nr. 2021-CIEN-000070-01. Gipuzkoa Next) for financial support.

* diego.pena@usc.es

† wmbgalea@ehu.eus

‡ ji.pascual@nanogune.eu

- [1] Young-Woo Son, Marvin L. Cohen, and Steven G. Louie, “Energy gaps in graphene nanoribbons,” *Physical Review Letters* **97**, 216803 (2006).
- [2] Li Yang, Cheol-Hwan Park, Young-Woo Son, Marvin L. Cohen, and Steven G. Louie, “Quasiparticle energies and band gaps in graphene nanoribbons,” *Physical Review Letters* **99**, 186801 (2007).
- [3] Oleg V. Yazyev, Rodrigo B. Capaz, and Steven G. Louie, “Theory of magnetic edge states in chiral graphene nanoribbons,” *Physical Review B* **84**, 115406 (2011).
- [4] Yen-Chia Chen, Ting Cao, Chen Chen, Zahra Pedramrazi, Danny Haberer, Dimas G De Oteyza, Felix R Fischer, Steven G Louie, and Michael F Crommie, “Molecular bandgap engineering of bottom-up synthesized graphene nanoribbon heterojunctions,” *Nature nanotechnology* **10**, 156–160 (2015).
- [5] Leopold Talirz, Hajo Söde, Shigeki Kawai, Pascal Ruffieux, Ernst Meyer, Xinliang Feng, Klaus Müllen, Roman Fasel, Carlo Antonio Pignedoli, and Daniele

- Passerone, “Band gap of atomically precise graphene nanoribbons as a function of ribbon length and termination,” *ChemPhysChem* **20**, 2348–2353 (2019).
- [6] Jingcheng Li, Sofia Sanz, Nestor Merino-Díez, Manuel Vilas-Varela, Aran Garcia-Lekue, Martina Corso, Dimas G. de Oteyza, Thomas Frederiksen, Diego Peña, and Jose Ignacio Pascual, “Topological phase transition in chiral graphene nanoribbons: from edge bands to end states,” *Nature Communications* **12**, 5538 (2021).
- [7] Jinming Cai, Pascal Ruffieux, Rached Jaafar, Marco Bieri, Thomas Braun, Stephan Blankenburg, Matthias Muoth, Ari P. Seitsonen, Moussa Saleh, Xinliang Feng, Klaus Müllen, and Roman Fasel, “Atomically precise bottom-up fabrication of graphene nanoribbons,” *Nature* **466**, 470–473 (2010).
- [8] Daniel J. Rizzo, Gregory Veber, Ting Cao, Christopher Bronner, Ting Chen, Fangzhou Zhao, Henry Rodriguez, Steven G. Louie, Michael F. Crommie, and Felix R. Fischer, “Topological band engineering of graphene nanoribbons,” *Nature* **560**, 204–208 (2018).
- [9] Oliver Gröning, Shiyong Wang, Xuelin Yao, Carlo A. Pignedoli, Gabriela Borin Barin, Colin Daniels, Andrew Cupo, Vincent Meunier, Xinliang Feng, Akimitsu Narita, Klaus Müllen, Pascal Ruffieux, and Roman Fasel, “Engineering of robust topological quantum phases in graphene nanoribbons,” *Nature* **560**, 209–213 (2018).
- [10] Sylvain Clair and Dimas G de Oteyza, “Controlling a chemical coupling reaction on a surface: tools and strategies for on-surface synthesis,” *Chemical reviews* **119**, 4717–4776 (2019).
- [11] Wei L. Wang, Sheng Meng, and Efthimios Kaxiras, “Graphene nanoflakes with large spin,” *Nano Letters* **8**, 241–245 (2008).
- [12] Wei L. Wang, Oleg V. Yazyev, Sheng Meng, and Efthimios Kaxiras, “Topological frustration in graphene nanoflakes: Magnetic order and spin logic devices,” *Physical Review Letters* **102**, 157201 (2009).
- [13] Shuang Wu, Bing Liu, Cheng Shen, Si Li, Xiaochun Huang, Xiaobo Lu, Peng Chen, Guole Wang, Duoming Wang, Mengzhou Liao, Jing Zhang, Tingting Zhang, Shuopei Wang, Wei Yang, Rong Yang, Dongxia Shi, Kenji Watanabe, Takashi Taniguchi, Yugui Yao, Weihua Wang, and Guangyu Zhang, “Magnetotransport properties of graphene nanoribbons with zigzag edges,” *Physical Review Letters* **120**, 216601 (2018).
- [14] Ting Cao, Fangzhou Zhao, and Steven G. Louie, “Topological phases in graphene nanoribbons: Junction states, spin centers, and quantum spin chains,” *Physical Review Letters* **119**, 076401 (2017).
- [15] Jingcheng Li, Sofia Sanz, Martina Corso, Deung Jang Choi, Diego Peña, Thomas Frederiksen, and Jose Ignacio Pascual, “Single spin localization and manipulation in graphene open-shell nanostructures,” *Nature Communications* **10**, 200 (2019).
- [16] Shantanu Mishra, Doreen Beyer, Kristjan Eimre, Shawlienu Kezilebieke, Reinhard Berger, Oliver Gröning, Carlo A. Pignedoli, Klaus Müllen, Peter Liljeroth, Pascal Ruffieux, Xinliang Feng, and Roman Fasel, “Topological frustration induces unconventional magnetism in a nanographene,” *Nature Nanotechnology* **15**, 22–28 (2020).
- [17] Shantanu Mishra, Doreen Beyer, Reinhard Berger, Junzhi Liu, Oliver Gröning, José I Urgel, Klaus Müllen, Pascal Ruffieux, Xinliang Feng, and Roman Fasel, “Topological defect-induced magnetism in a nanographene,” *Journal of the American Chemical Society* **142**, 1147–1152 (2020).
- [18] James Lawrence, Pedro Brandimarte, Alejandro Berdonces-Layunta, Mohammed S. G. Mohammed, Abhishek Grewal, Christopher C. Leon, Daniel Sánchez-Portal, and Dimas G. de Oteyza, “Probing the magnetism of topological end states in 5-armchair graphene nanoribbons,” *ACS Nano* **14**, 4499–4508 (2020).
- [19] Shantanu Mishra, Doreen Beyer, Kristjan Eimre, Ricardo Ortiz, Joaquín Fernández-Rossier, Reinhard Berger, Oliver Gröning, Carlo A. Pignedoli, Roman Fasel, Xinliang Feng, and Pascal Ruffieux, “Collective all-carbon magnetism in triangulene dimers,” *Angewandte Chemie International Edition* **59**, 12041–12047 (2020).
- [20] Borja Cirera, Ana Sánchez-Grande, Bruno de la Torre, José Santos, Shayan Edalatmanesh, Eider Rodríguez-Sánchez, Koen Lauwaet, Benjamin Mallada, Radek Zbořil, Rodolfo Miranda, Oliver Gröning, Pavel Jelínek, Nazario Martín, and David Eciija, “Tailoring topological order and π -conjugation to engineer quasi-metallic polymers,” *Nature Nanotechnology* **15**, 437–443 (2020), [arXiv:1911.05514](https://arxiv.org/abs/1911.05514).
- [21] Jingcheng Li, Sofia Sanz, Jesus Castro-Esteban, Manuel Vilas-Varela, Niklas Friedrich, Thomas Frederiksen, Diego Peña, and Jose Ignacio Pascual, “Uncovering the triplet ground state of triangular graphene nanoflakes engineered with atomic precision on a metal surface,” *Physical Review Letters* **124**, 177201 (2020).
- [22] Ana Sánchez-Grande, José I Urgel, Aleš Cahlk, José Santos, Shayan Edalatmanesh, Eider Rodríguez-Sánchez, Koen Lauwaet, Pingo Mutombo, Dana Nachtigallová, Reed Nieman, *et al.*, “Diradical organic one-dimensional polymers synthesized on a metallic surface,” *Angewandte Chemie International Edition* **59**, 17594–17599 (2020).
- [23] Niklas Friedrich, Pedro Brandimarte, Jingcheng Li, Shohei Saito, Shigehiro Yamaguchi, Iago Pozo, Diego Peña, Thomas Frederiksen, Aran Garcia-Lekue, Daniel Sánchez-Portal, and José Ignacio Pascual, “Magnetism of topological boundary states induced by boron substitution in graphene nanoribbons,” *Physical Review Letters* **125**, 146801 (2020).
- [24] Yuqiang Zheng, Can Li, Chengyang Xu, Doreen Beyer, Xinlei Yue, Yan Zhao, Guanyong Wang, Dandan Guan, Yaoyi Li, Hao Zheng, Canhua Liu, Junzhi Liu, Xiaogun Wang, Weidong Luo, Xinliang Feng, Shiyong Wang, and Jinfeng Jia, “Designer spin order in diradical nanographenes,” *Nature Communications* **11**, 6076 (2020).
- [25] Ana Sánchez-Grande, José I Urgel, Libor Veis, Shayan Edalatmanesh, José Santos, Koen Lauwaet, Pingo Mutombo, José M Gallego, Jiri Brabec, Pavel Beran, *et al.*, “Unravelling the open-shell character of peripentacene on au (111),” *The journal of physical chemistry letters* **12**, 330–336 (2020).
- [26] Shantanu Mishra, Xuelin Yao, Qiang Chen, Kristjan Eimre, Oliver Gröning, Ricardo Ortiz, Marco Di Giovannantonio, Juan Carlos Sancho-García, Joaquín Fernández-Rossier, Carlo A. Pignedoli, Klaus Müllen, Pascal Ruffieux, Akimitsu Narita, and Roman Fasel, “Large magnetic exchange coupling in rhombus-shaped nanographenes with zigzag periphery,” *Nature Chemistry* **13**, 581–586 (2021).

- [27] Elia Turco, Shantanu Mishra, Jason Melidonie, Kristjan Eimre, Sebastian Obermann, Carlo A Pignedoli, Roman Fasel, Xinliang Feng, and Pascal Ruffieux, “On-surface synthesis and characterization of super-nonazethrene,” *The journal of physical chemistry letters* **12**, 8314–8319 (2021).
- [28] Shantanu Mishra, Gonalo Catarina, Fupeng Wu, Ricardo Ortiz, David Jacob, Kristjan Eimre, Ji Ma, Carlo A. Pignedoli, Xinliang Feng, Pascal Ruffieux, Joaqu n Fern ndez-Rossier, and Roman Fasel, “Observation of fractional edge excitations in nanographene spin chains,” *Nature* **598**, 287–292 (2021), 2105.09102.
- [29] Jeremy Hieulle, Silvia Castro, Niklas Friedrich, Alessio Vegliante, Francisco Romero Lara, Sof a Sanz, Dulce Rey, Martina Corso, Thomas Frederiksen, Jose Ignacio Pascual, and Diego Pe a, “On-surface synthesis and collective spin excitations of a triangulene-based nanostar,” *Angewandte Chemie International Edition* **60**, 25224–25229 (2021).
- [30] Tao Wang, Sof a Sanz, Jes s Castro-Esteban, James Lawrence, Alejandro Berdonces-Layunta, Mohammed S. G. Mohammed, Manuel Vilas-Varela, Martina Corso, Diego Pe a, Thomas Frederiksen, and Dimas G. de Oteyza, “Magnetic interactions between radical pairs in chiral graphene nanoribbons,” *Nano Letters* **22**, 164–171 (2021).
- [31] Kalyan Biswas, Jos  I Urgel, MR Ajayakumar, Ji Ma, Ana S nchez-Grande, Shayan Edalatmanesh, Koen Lauwaet, Pingo Mutombo, Jos  M Gallego, Rodolfo Miranda, *et al.*, “Synthesis and characterization of perihaptacene on a metallic surface,” *Angewandte Chemie*, e202114983 (2022).
- [32] Tao Wang, Alejandro Berdonces-Layunta, Niklas Friedrich, Manuel Vilas-Varela, Jan Patrick Calupitan, Jose Ignacio Pascual, Diego Pe a, David Casanova, Martina Corso, and Dimas G. de Oteyza, “Aza-triangulene: On-surface synthesis and electronic and magnetic properties,” *Journal of the American Chemical Society* **144**, 4522–4529 (2022).
- [33] Sujoy Karan, Tobias Frank, Tobias Preis, Jonathan Eroms, Jaroslav Fabian, Ferdinand Evers, and Jascha Repp, “Interplay of boundary states of graphene nanoribbons with a kondo impurity,” *Physical Review B* **105**, 205410 (2022).
- [34] Shaotang Song, Pei Wen Ng, Shayan Edalatmanesh, Andr s Pinar Sol , Xinnan Peng, Jindřich Koloren , Zdenka Sosnov , Oleksander Stetsovych, Jie Su, Jing Li, Hongli Sun, Alexander Liebig, Chenliang Su, Jishan Wu, Franz J. Giessibl, Pavel Jelinek, Chunyan Chi, and Jiong Lu, “Designer magnetic topological graphene nanoribbons,” (2022).
- [35] Jingcheng Li, Niklas Friedrich, Nestor Merino, Dimas G. de Oteyza, Diego Pe a, David Jacob, and Jose Ignacio Pascual, “Electrically addressing the spin of a magnetic porphyrin through covalently connected graphene electrodes,” *Nano Letters* **19**, 3288–3294 (2019).
- [36] Alexander Tzalenchuk, Samuel Lara-Avila, Alexei Kalaboukhov, Sara Paolillo, Mikael Syv jarvi, Rositsa Yakimova, Olga Kazakova, T. J.B.M. Janssen, Vladimir Fal’Ko, and Sergey Kubatkin, “Towards a quantum resistance standard based on epitaxial graphene,” *Nature Nanotechnology* **5**, 186–189 (2010).
- [37] Johannes Aprozanz, Stephen R. Power, Pantelis Bampoulis, Stephan Roche, Antti Pekka Jauho, Harold J.W. Zandvliet, Alexei A. Zakharov, and Christoph Tegenkamp, “Ballistic tracks in graphene nanoribbons,” *Nature Communications* **9**, 2–7 (2018).
- [38] Hrag Karakachian, T. T.Nhung Nguyen, Johannes Aprozanz, Alexei A. Zakharov, Rositsa Yakimova, Philipp Rosenzweig, Craig M. Polley, Thiagarajan Balasubramanian, Christoph Tegenkamp, Stephen R. Power, and Ulrich Starke, “One-dimensional confinement and width-dependent bandgap formation in epitaxial graphene nanoribbons,” *Nature Communications* **11**, 1–8 (2020).
- [39] Ryan R. Cloke, Tomas Marangoni, Giang D. Nguyen, Trinity Joshi, Daniel J. Rizzo, Christopher Bronner, Ting Cao, Steven G. Louie, Michael F. Crommie, and Felix R. Fischer, “Site-specific substitutional boron doping of semiconducting armchair graphene nanoribbons,” *Journal of the American Chemical Society* **137**, 8872–8875 (2015).
- [40] Shigeki Kawai, Shohei Saito, Shinichiro Osumi, Shigehiro Yamaguchi, Adam S. Foster, Peter Spijker, and Ernst Meyer, “Atomically controlled substitutional boron-doping of graphene nanoribbons,” *Nature Communications* **6**, 8098 (2015).
- [41] Eduard Carbonell-Sanrom , Pedro Brandimarte, Richard Balog, Martina Corso, Shigeki Kawai, Aran Garcia-Lekue, Shohei Saito, Shigehiro Yamaguchi, Ernst Meyer, Daniel S nchez-Portal, and Jose Ignacio Pascual, “Quantum dots embedded in graphene nanoribbons by chemical substitution,” *Nano Letters* **17**, 50–56 (2017).
- [42] Shigeki Kawai, Soichiro Nakatsuka, Takuji Hatakeyama, R my Pawlak, Tobias Meier, John Tracey, Ernst Meyer, and Adam S. Foster, “Multiple heteroatom substitution to graphene nanoribbon,” *Science Advances* **4**, 1–8 (2018).
- [43] Eduard Carbonell-Sanrom , Aran Garcia-Lekue, Martina Corso, Guillaume Vasseur, Pedro Brandimarte, Jorge Lobo-Checa, Dimas G. de Oteyza, Jingcheng Li, Shigeki Kawai, Shohei Saito, Shigehiro Yamaguchi, J. Enrique Ortega, Daniel S nchez-Portal, and Jose Ignacio Pascual, “Electronic properties of substitutionally boron-doped graphene nanoribbons on a au(111) surface,” *The Journal of Physical Chemistry C* **122**, 16092–16099 (2018).
- [44] Boris V. Senkovskiy, Dmitry Yu Usachov, Alexander V. Fedorov, Tomas Marangoni, Danny Haberer, Cesare Tresca, Gianni Profeta, Vasile Caciuc, Shigeru Tsukamoto, Nicolae Atodiresei, Niels Ehlen, Chaoyu Chen, Jos  Avila, Maria C. Asensio, Andrei Yu Varykhalov, Alexei Nefedov, Christof W ll, Timur K. Kim, Moritz Hoesch, Felix R. Fischer, and Alexander Gr neis, “Boron-doped graphene nanoribbons: Electronic structure and raman fingerprint,” *ACS Nano* **12**, 7571–7582 (2018).
- [45] Peina Zhang, Xinlu Li, Jianting Dong, Meng Zhu, Fanxing Zheng, and Jia Zhang, “ π -magnetism and spin-dependent transport in boron pair doped armchair graphene nanoribbons,” *Applied Physics Letters* **120**, 132406 (2022).
- [46] Massimo Fritton, Katrin Otte, Jonas Bj rk, Pronay Kumar Biswas, Wolfgang M Heckl, Michael Schmittel, and Markus Lackinger, “The influence of ortho-methyl substitution in organometallic self-assembly - a comparative study on cu (111) vs. ag (111),” *Chemical Communications* **54**, 9745–9748 (2018).

- [47] Dennis Barton, Hong-Ying Gao, Philipp Alexander Held, Armido Studer, Harald Fuchs, Nikos L. Doltsinis, and Johannes Neugebauer, "Formation of organometallic intermediate states in on-surface ullmann couplings," *Chemistry - A European Journal* **23**, 6190–6197 (2017).
- [48] Leif Lafferentz, Francisco Ample, Hao Yu, Stefan Hecht, Christian Joachim, and Leonhard Grill, "Conductance of a single conjugated polymer as a continuous function of its length," *Science* **323**, 1193–1197 (2009).
- [49] Matthias Koch, Francisco Ample, Christian Joachim, and Leonhard Grill, "Voltage-dependent conductance of a single graphene nanoribbon," *Nature Nanotechnology* **7**, 713–717 (2012).
- [50] Peter H. Jacobse, Mark J. J. Mangnus, Stephan J. M. Zevenhuizen, and Ingmar Swart, "Mapping the conductance of electronically decoupled graphene nanoribbons," *ACS Nano* **12**, 7048–7056 (2018).
- [51] Michael C. Chong, Nasima Afshar-Imani, Fabrice Scheurer, Claudia Cardoso, Andrea Ferretti, Deborah Prezzi, and Guillaume Schull, "Bright electroluminescence from single graphene nanoribbon junctions," *Nano Letters* **18**, 175–181 (2018).
- [52] Jeremy M. Beebe, Vincent B. Engelkes, Larry L. Miller, and C. Daniel Frisbie, "Contact resistance in metal-molecule-metal junctions based on aliphatic sams: Effects of surface linker and metal work function," *Journal of the American Chemical Society* **124**, 11268–11269 (2002).
- [53] Latha Venkataraman, Jennifer E Klare, Iris W Tam, Colin Nuckolls, Mark S Hybertsen, and Michael L Steigerwald, "Single-molecule circuits with well-defined molecular conductance," *Nano Letters* **6**, 458–462 (2006).
- [54] Gaël Reecht, Fabrice Scheurer, Virginie Speisser, Yannick J. Dappe, Fabrice Mathevet, and Guillaume Schull, "Electroluminescence of a Polythiophene Molecular Wire Suspended between a Metallic Surface and the Tip of a Scanning Tunneling Microscope," *Physical Review Letters* **112**, 047403 (2014).
- [55] H O Frota, "Shape of the Kondo resonance," *Physical Review B* **45**, 1096–1099 (1992).
- [56] Jun Kondo, "Resistance minimum in dilute magnetic alloys," *Progress of Theoretical Physics* **32**, 37–49 (1964).
- [57] P. W. Anderson, "Theory of localized magnetic states in metals," *Journal of Applied Physics* **37**, 1194 (1966).
- [58] Nicolas Roch, Serge Florens, Theo A. Costi, Wolfgang Wernsdorfer, and Franck Balestro, "Observation of the underscreened kondo effect in a molecular transistor," *Physical Review Letters* **103**, 197202 (2009).
- [59] Markus Ternes, Andreas J Heinrich, and Wolf dieter Schneider, "Spectroscopic manifestations of the kondo effect on single adatoms," *Journal of Physics: Condensed Matter* **21**, 053001 (2009).
- [60] Leo Gross, Z L Wang, D Ugarte, Fabian Mohn, Nikolaj Moll, W a Heer, P Vincent, Peter Liljeroth, C Journet, Gerhard Meyer, V T Binh, M Poot, H S J Van Der Zant, A Aguasca, A Bachtold, K Kim, A Zettl, P Hung, H W C Postma, M Bockrath, X Blase, and S Roche, "The Chemical Structure of a Molecule Resolved by Atomic Force Microscopy," *Science* **325**, 1110–4 (2009).
- [61] Georgy Kichin, Christian Weiss, Christian Wagner, F. Stefan Tautz, and Ruslan Temirov, "Single molecule and single atom sensors for atomic resolution imaging of chemically complex surfaces," *Journal of the American Chemical Society* **133**, 16847–16851 (2011).
- [62] Xinnan Peng, Harshitra Mahalingam, Shaoqiang Dong, Pingo Mutombo, Jie Su, Mykola Telychko, Shaotang Song, Pin Lyu, Pei Wen Ng, Jishan Wu, Pavel Jelínek, Chunyan Chi, Aleksandr Rodin, and Jiong Lu, "Visualizing designer quantum states in stable macrocycle quantum corrals," *Nature Communications* **12**, 5895 (2021).
- [63] Shadi Fatayer, Florian Albrecht, Ivano Tavernelli, Mats Persson, Nikolaj Moll, and Leo Gross, "Probing molecular excited states by atomic force microscopy," *Physical Review Letters* **126**, 176801 (2021).
- [64] Ignacio Horcas, Rs Fernández, JM Gomez-Rodriguez, JWSX Colchero, JWSXM Gómez-Herrero, and AM Baro, "Wsxm: a software for scanning probe microscopy and a tool for nanotechnology," *Review of scientific instruments* **78**, 013705 (2007).
- [65] J. D. Hunter, "Matplotlib: A 2d graphics environment," *Computing in Science & Engineering* **9**, 90–95 (2007).
- [66] Peter Kovesi, "Good colour maps: How to design them," arXiv preprint arXiv:1509.03700 (2015).
- [67] E. Artacho, D. Sánchez-Portal, P. Ordejón, A. García, and J.M. Soler, "Linear-scaling ab-initio calculations for large and complex systems," *physica status solidi (b)* **215**, 809–817 (1999).
- [68] José M Soler, Emilio Artacho, Julian D Gale, Alberto García, Javier Junquera, Pablo Ordejón, and Daniel Sánchez-Portal, "The SIESTA method forab initioordermaterials simulation," *Journal of Physics: Condensed Matter* **14**, 2745–2779 (2002).
- [69] M. Dion, H. Rydberg, E. Schröder, D. C. Langreth, and B. I. Lundqvist, "Van der waals density functional for general geometries," *Physical Review Letters* **92** (2004).
- [70] Jiří Klimeš, David R Bowler, and Angelos Michaelides, "Chemical accuracy for the van der waals density functional," *Journal of Physics: Condensed Matter* **22**, 022201 (2009).
- [71] N. Troullier and José Luriaas Martins, "Efficient pseudopotentials for plane-wave calculations," *Physical Review B* **43**, 1993–2006 (1991).

Addressing electron spins embedded in metallic graphene nanoribbons - Supporting Information

Niklas Friedrich,¹ Rodrigo E. Menchón,² Iago Pozo,³ Jeremy Hieulle,¹ Alessio Vegliante,¹ Jingcheng Li,¹ Daniel Sánchez-Portal,^{2,4} Diego Peña,^{3,*} Aran Garcia-Lekue,^{2,5,†} and José Ignacio Pascual^{1,5,‡}

¹*CIC nanoGUNE-BRTA, 20018 Donostia-San Sebastián, Spain*

²*Donostia International Physics Center (DIPC), 20018 Donostia-San Sebastián, Spain*

³*CiQUS, Centro Singular de Investigación en Química Biolóxica e Materiais Moleculares, 15705 Santiago de Compostela, Spain*

⁴*Centro de Física de Materiales CSIC-UPV/EHU, 20018 Donostia-San Sebastián, Spain*

⁵*Ikerbasque, Basque Foundation for Science, 48013 Bilbao, Spain*

(Dated: June 16, 2022)

CONTENTS

Synthesis of the molecular precursor	2
General methods	2
Synthesis of precursor molecule	2
Complementary experimental data	4
Conductance-Distance Plot	4
Transition from Kondo to IET-regime	5
The Four Sites Fermi-Hubbard Model	6
DFT Calculations	7
Magnetic States in Finite Ribbons	7
Magnetic Ground State of the Periodic 2B-575*-aGNR	8
Continuous Boron Substitution and Boron Bands Origin	9
Influence of the Ribbon Width Modulation	11
Complete Set of Bands of the 2B-575-aGNR Near the Fermi Level	12
Bibliography	13
	13

SYNTHESIS OF THE MOLECULAR PRECURSOR

General methods

Reactions were carried out under argon using oven-dried glassware. Et₂O and toluene were purified in a MBraun SPS-800 Solvent Purification System. 9,10-dibromo-9,10-diboraanthracene (DBA) was prepared following a published procedure [1] and stored in a glovebox. Other commercial reagents were purchased from ABCR GmbH or Sigma-Aldrich and were used without further purification. TLC was performed on Merck silica gel 60 F254 and chromatograms were visualized with UV light (254 and 365 nm). Column chromatography was performed on Merck silica gel 60 (ASTM 230-400 mesh). ¹H NMR spectra were recorded at 300 MHz (Varian Mercury-300 instrument).

Synthesis of precursor molecule

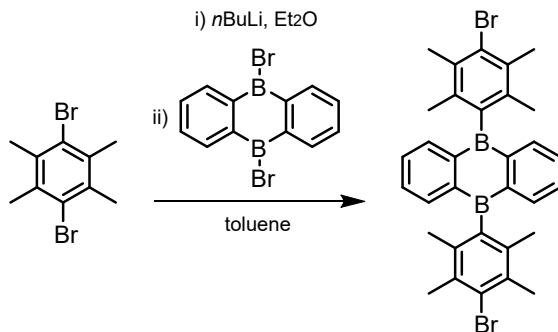


FIG. 1. Synthetic route to obtain the boron-doped GNR precursor.

To a solution of 9,10-dibromodurene (174 mg, 0.60 mmol) in dry Et₂O (0.04 M) at -78°C in a Schlenk tube, *n*-BuLi (2.5 M in hexane, 0.63 mmol) was dropwise added. Subsequently, the reaction mixture was stirred at 0°C for 20 min and cooled again to -78°C . Then, another solution of 9,10-dibromo-9,10-diboraanthracene (DBA, 100 mg, 0.30 mmol) in dry toluene (0.02 M) was dropwise added at -78°C and allowed to warm up to $\text{rt}^{\circ}\text{C}$ for 18 h. Then, the solvent was removed under reduced pressure and the crude was purified by column chromatography (SiO₂, CHCl₃:hexane 1:1, R_f = 0.9). The solid obtained was washed with hexane and centrifuged affording 5,10-bis(4-bromo-2,3,5,6-tetramethylphenyl)-5,10-dihydroboranthrene as a white solid (27 mg, m.p.: > 350 decomp., 15% yield). ¹H NMR (300 MHz, CDCl₃): 7.59 (m, 4H), 7.47 (m, 4H), 2.44 (s, 12H), 2.03 (s, 12H) ppm. MS (APCI), *m/z*: 598 (M⁺, 100). HRMS (APCI), *m/z* found: 596.1064 (calc. for C₃₂H₃₂B₂Br₂: 596.1051).

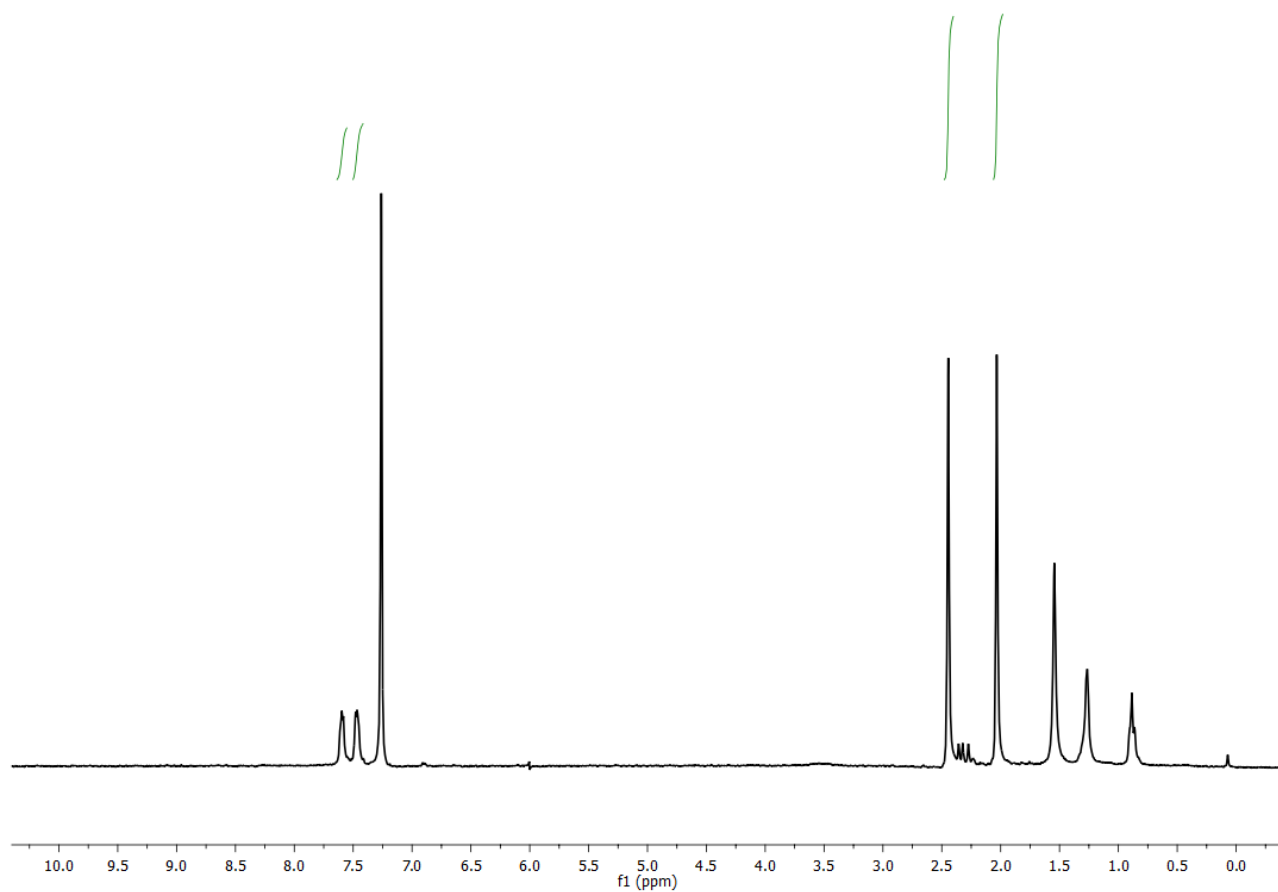


FIG. 2. ^1H NMR of the boron-doped GNR precursor in CDCl_3 at room temperature

COMPLEMENTARY EXPERIMENTAL DATA

Conductance - Distance Plot

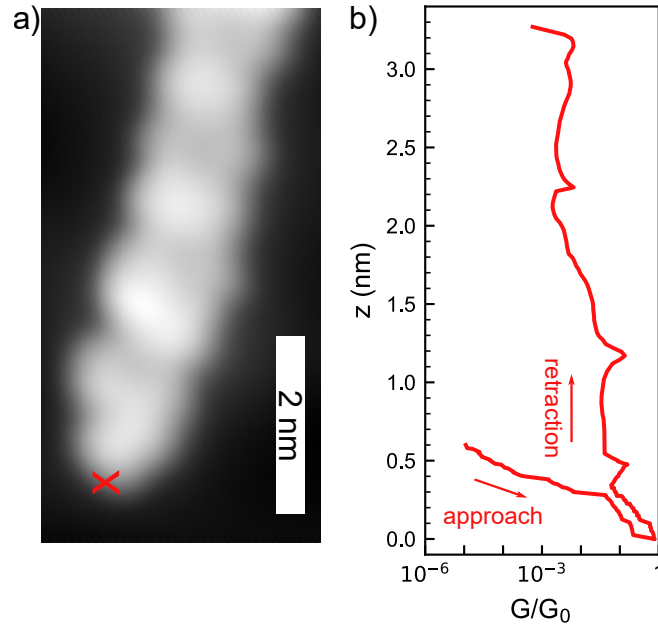


FIG. 3. (a) STM topography image ($V = -300$ mV, $I = 30$ pA) of a 2B-575-aGNR. It is the same image as Figure 3b of the main text and only shown for reference. (b) $G(z, V = 10$ mV) for the GNR presented in (a). The data was recorded simultaneously to the differential conductance map presented in Figure 3a.

The $G(z)$ retraction curve recorded during lifting the ribbon presented in the main manuscript in Figure 3 initially reaches $G(z) \sim 0.1G_0$. The conductance lowers with increasing tip sample separation, but does not follow the exponential decay characteristic of semi-conducting ribbons.

Transition from Kondo to IET-regime

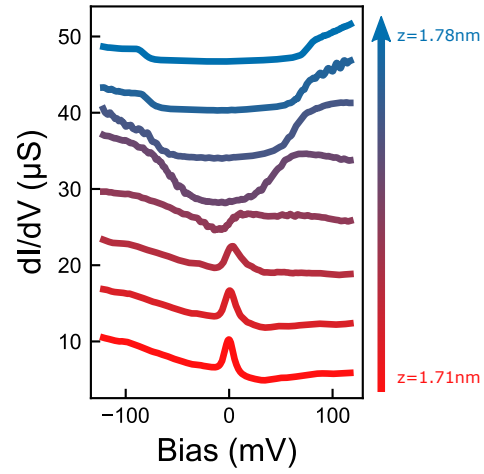


FIG. 4. A Stack of differential conductance spectra taken in steps of $\Delta z = 10$ pm shows the continuous transition from the Kondo resonance to a IET excitation. Data corresponding to Figure 4e of the main manuscript. The spectra are offset by $6.6 \mu\text{S}$ for clarity.

The ribbon presented in Figure 4 of the main manuscript undergoes a transition from Kondo regime to an IET regime upon tip retraction starting from $z \sim 1.7$ nm. The transition takes place smoothly during few tens of pm.

THE FOUR SITES FERMI-HUBBARD MODEL

The finite-size Fermi-Hubbard model with n sites has the following Hamiltonian:

$$\hat{H} = \sum_{j=1}^{n-1} \sum_{\sigma=\uparrow,\downarrow} t \left(\hat{c}_{j+1,\sigma}^\dagger \hat{c}_{j,\sigma} + \hat{c}_{j,\sigma}^\dagger \hat{c}_{j+1,\sigma} \right) + \sum_{j=1}^n U \hat{n}_{j,\uparrow} \hat{n}_{j,\downarrow}$$

where each $\hat{c}_{j,\sigma}^\dagger$ ($\hat{c}_{j,\sigma}$) is the fermionic creation (annihilation) operator of site j and spin σ , $\hat{n}_{j,\sigma} = \hat{c}_{j,\sigma}^\dagger \hat{c}_{j,\sigma}$, U is the Hubbard on-site repulsion between two electrons and t is related to the kinetic energy of an electron hopping from one site to an adjacent site. A schematic illustration of the structure is shown in the main manuscript in Figure 4g. Approximate values of the two parameters were obtained from the band structure shown in Figure 4f of the main manuscript. The energy spectrum and eigenstates of the system were obtained through exact diagonalization.

To analyze the stability of the Fermi-Hubbard model with respect to changes of U , we have considered U values ranging from 0 to $2t$. The results are presented in Figure 5. Within this energy range, no qualitative change of behaviour is observed. The energy difference between the ground state and the two excited states remains in the order of t , indicating that this is the relevant energy scale for the experimentally observed excitations. Furthermore, the energy scale of the first excited states of the model is robust against changes in the number of electrons. Excitation energies were calculated for one, two and three electrons in the model (Figure 6). We find that the excitation energies match reasonably well with the experimental data in all cases.

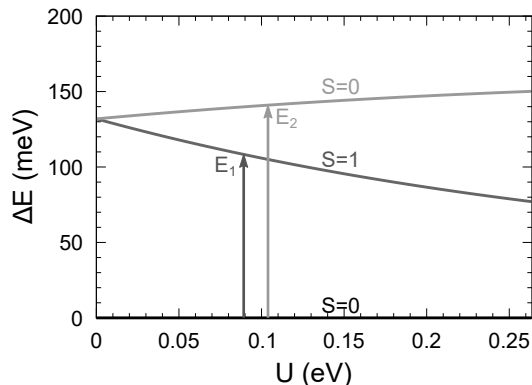


FIG. 5. Excitation energy ΔE obtained from the energy spectrum of the Fermi-Hubbard model as a function of U in the two electron model with $t = 133.9$ meV.

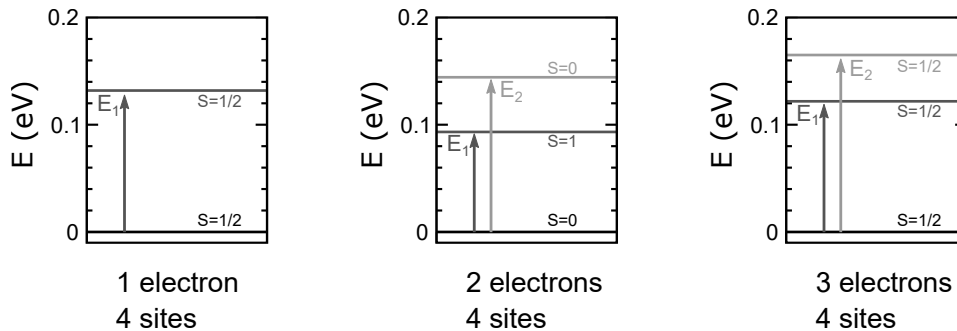


FIG. 6. Excitation spectrum obtained from the four-site model Hamiltonian with one, two and three electrons (left to right) for $U = 155.9$ meV and $t = 131.9$ meV. For an odd number of electrons, there are only doublet-doublet excitations in this energy range. For an even number of electrons, there are both singlet-triplet and singlet-singlet excitations. Note that the excitation energy increases when going from two to three electrons.

DFT CALCULATIONS

Magnetic States in Finite Ribbons

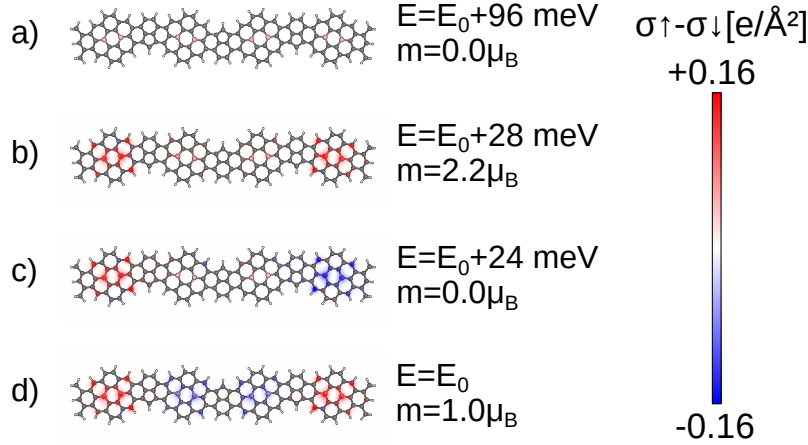


FIG. 7. Spin polarization density for the finite 2B-575*-aGNR converged for different spin configurations. (a) Non-spin-polarized solution. (b) The spin in all 2B-units aligns. There is a stronger spin-polarization present at the termini. (c) The spin in the termini anti-aligns, while there is hardly any spin-polarization localized around the two inner 2B-units. (d) Ground state of the system. The spins localized in the termini align with each other and anti-align with the spin around the inner 2B-units. The spin-polarization on the two inner 2B-units does not fully compensate the magnetic moments localized at the termini.

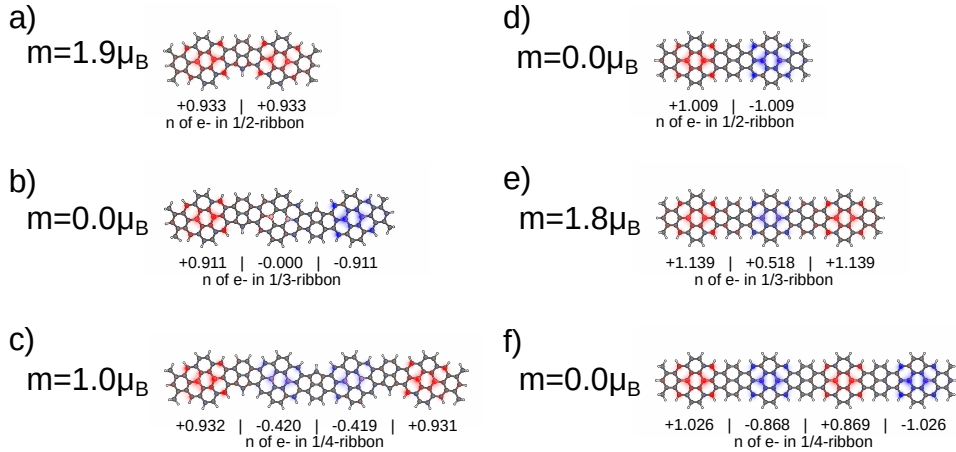


FIG. 8. Spin polarization densities of the energetic ground state of each finite 2B-575*-aGNR and 2B-575-aGNR. (a),(b),(c) for finite 2B-575*-aGNR of 2, 3 and 4 2B-units, respectively. (d),(e),(f) for finite 2B-575-aGNR of 2, 3 and 4 2B-units, respectively.

Magnetic Ground State of the Periodic 2B-575*-aGNR

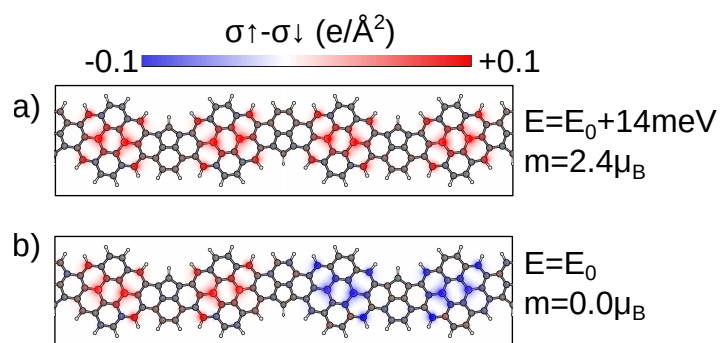


FIG. 9. Spin polarization density for the periodic 2B-575*-aGNR using a doubled supercell. (a) Aligned solution. (b) Anti-aligned solution. The anti-aligned groundstate is 14 meV lower in energy.

Continuous Boron Substitution and Boron Bands Origin

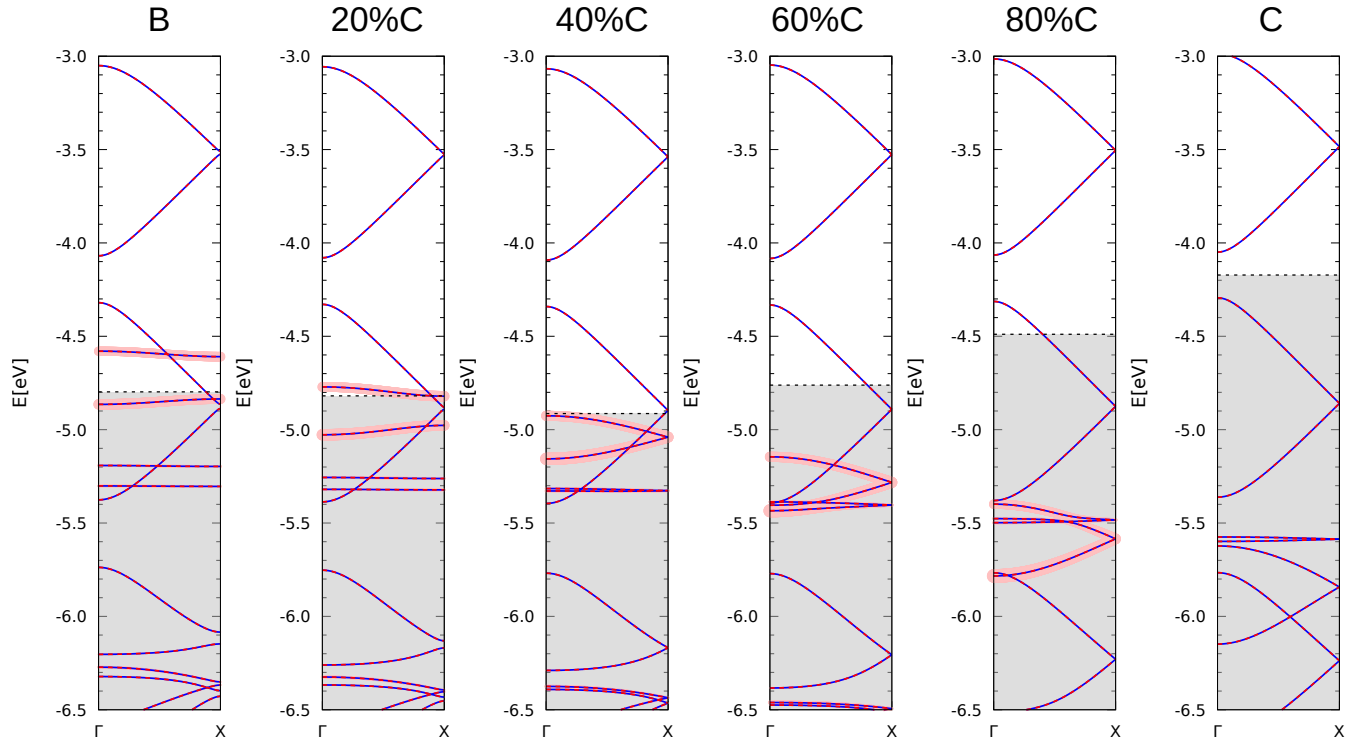


FIG. 10. Electronic band structures of periodic 2B-575-aGNR as obtained from virtual crystal calculations with synthetic atoms (created as a mixture of Boron and Carbon) at the substitutional doping sites. Boron character of the bands is indicated by a pink shadow.

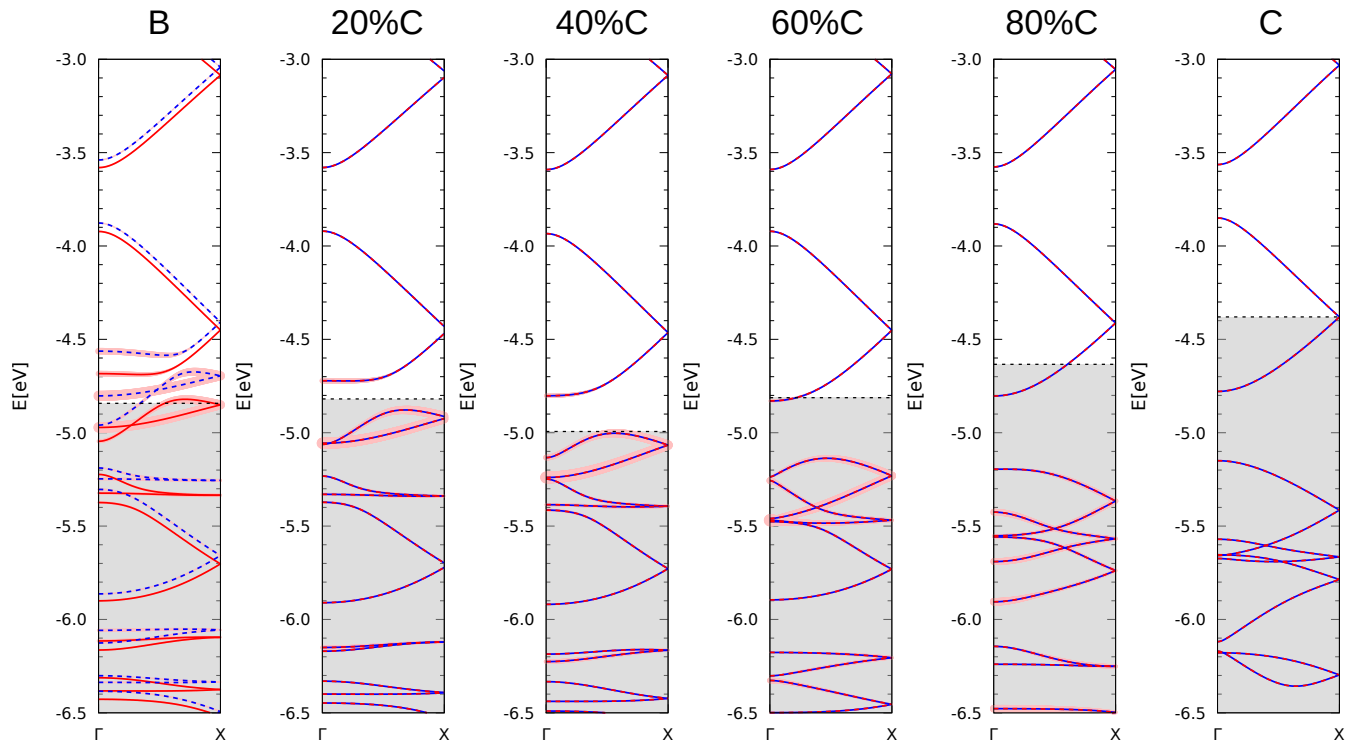


FIG. 11. Electronic band structures of periodic 2B-575*-aGNR as obtained from virtual crystal calculations with synthetic atoms (created as a mixture of Boron and Carbon) at the substitutional doping sites. Boron character of the bands is indicated by a pink shadow.

Influence of the Ribbon Width Modulation

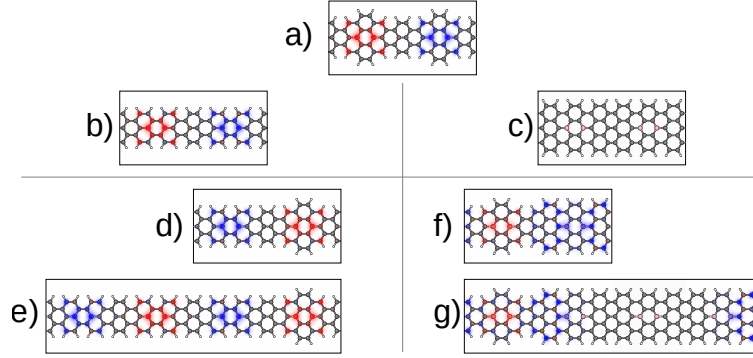


FIG. 12. Spin polarization densities corresponding to different periodic systems with the same distance between substitutional doping sites. (a) 2B-575-aGNR, (b) 2B-5-aGNR and (c) 2B-7-aGNR. It is worth pointing out that 2B-5-aGNR exhibits a local magnetization very similar to the one featured in 2B-575-aGNR whereas for the 2B-7-aGNR there is no local magnetization. Panels (d),(e),(f) and (g) show mixed systems, the combination of 2B-575-aGNR with the two other GNRs. (d) presents a system combining each one 2B-unit of a 2B-5-aGNR and a 2B-575-aGNR. It presents a magnetization similar to both of their parent systems. (e) presents a system combining three 2B-units of a 2B-5-aGNR with one of a 2B-575-aGNR. (f) presents a system combining one 2B-unit of a 2B-575-aGNR followed by one of a 2B-7-aGNR. The carbon atoms located in the 7-aGNR-segments contribute to the magnetization. (g) presents a system combining one 2B-unit of a 2B-575-aGNR followed by three of a 2B-7-aGNR. Local magnetization goes to zero for the 2B-7-aGNR unit located the furthest away from the 2B-575-aGNR.

Complete Set of Bands of the 2B-575-aGNR Near the Fermi Level

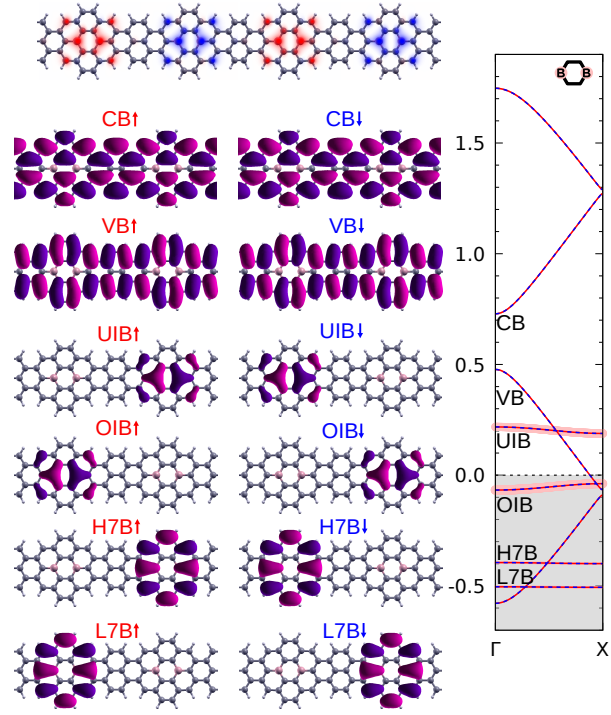


FIG. 13. DFT calculated wavefunctions at Γ for the bands near the Fermi level of the 2B-575-aGNR. The wavefunctions for the most dispersive bands (CB and VB) are identical for spin up and down cases. The weakly dispersive bands (UIB, OIB, H7B and L7B) exhibit different wavefunctions depending on the spin.

BIBLIOGRAPHY

* diego.pena@usc.es

† wmbgalea@ehu.eus

‡ ji.pascual@nanogune.eu

- [1] Bieller, S.; Zhang, F.; Bolte, M.; Bats, J. W.; Lerner, H.-W.; Wagner, M. Bitopic bis- and tris (1-pyrazolyl) borate ligands: syntheses and structural characterization. *Organometallics* **2004**, *23*, 2107–2113.